Accepted Manuscript

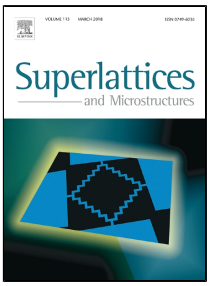

Effect of annealing temperature on structural, morphology and dielectric properties of $La_{0.75}Ba_{0.25}FeO_3$ perovskite

F.B. Abdallah, A. Benali, M. Triki, E. Dhahri, M.P.F. Graca, M.A. Valente

PII:	S0749-6036(18)30352-5
DOI:	10.1016/j.spmi.2018.03.048
Reference:	YSPMI 5578
To appear in:	*Superlattices and Microstructures*
Received Date:	19 February 2018
Revised Date:	16 March 2018
Accepted Date:	19 March 2018

Please cite this article as: F.B. Abdallah, A. Benali, M. Triki, E. Dhahri, M.P.F. Graca, M.A. Valente, Effect of annealing temperature on structural, morphology and dielectric properties of $La_{0.75}Ba_{0.25}FeO_3$ perovskite, *Superlattices and Microstructures* (2018), doi: 10.1016/j.spmi.2018.03.048

Effect of annealing temperature on structural, morphology and dielectric properties of $La_{0.75}Ba_{0.25}FeO_3$ perovskite

F.B. Abdallah, [*a] A. Benali, [a] M. Triki,[**a] E. Dhahri, [a] M. P. F. Graca[b] and M.A. Valente [b]

[a] Laboratoire de Physique Appliquée, Faculté des Sciences, B.P. 1171, 3000 Sfax, Université de Sfax, Tunisia.

[b] I3N and Physics Department, University of Aveiro, 3810-193 Aveiro, Portugal.

* abdallahfatma72@gmail.com

** mtriki_fss@yahoo.fr

Abstract:

The effect of annealing temperature on the structure, morphology and dielectric properties of $La_{0.75}Ba_{0.25}FeO_3$ compound prepared by the sol-gel method was investigated. The increase of the annealing temperature from 900 to 1100 °C, promotes an increase of the average grain size value. Two dielectric relaxations are detected using the dielectric modulus formalism, attributed to grain and grain boundary relaxations. This behavior was confirmed by both Nyquist and Argand's plots of dielectric impedance and Modulus results at different measuring temperatures. The ac conductivity could be described by Jonscher's power law revealing the presence of both overlapping large polaron tunneling and non-overlapping small polaron tunneling mechanisms.

***Keywords*:** Perovskite, Sol-gel, Impedance spectroscopy, Annealing effect, Ac conductivity

I. Introduction:

Now-a-days, a large number of perovskite oxides (with the general formula ABO_3) with different structural families are available with a wide variety of physical properties. Especially, Lanthanum orthoferrite $LaFeO_3$ is one of the most common perovskite-type oxide and has an orthorhombic structure with *Pnma* space group. Bulk $LaFeO_3$ is known to be antiferromagnetic with a Neel temperature of 740 K and it was largely used as solid oxide fuel cells [1, 2], catalysts [3], chemical sensors [4, 5], magnetic materials [6, 7] and oxygen permeation membranes [8, 9]. Many interesting observations on $LaFeO_3$ and La or Fe-site doped $LaFeO_3$ have been reported [10, 11]. It shows high electrical conductivity, outstanding thermal stability, high dielectric constant, low dielectric loss, moderate permittivity, polarizability, ferroelectricity and multiferroicity.

Dielectric spectroscopy is an important and powerful tool to study dielectric and conduction properties of complex perovskite oxides as it distinguishes between intrinsic (bulk) and extrinsic (grain-boundary, surface layer and electrode) contributions. Several studies have focused on the dielectric properties of the doped $LaFeO_3$. C. Chen et al. [12] reported that $LaFeO_3$ exhibits a colossal dielectric behavior and a Debye-like relaxation with activation energy of 0.237 eV. The relaxation was confirmed to be a polaronic relaxation. Currently, the existing dielectric investigations on this material were concentrated on the doped $LaFeO_3$. S. Chanda et al. [13] have studied the dielectric properties of $La_{1-x}Pr_xFeO_3$ nanocrystalline. They have found two semicircular arcs in complex impedance plot attributed to the grain and grain-boundary effects which are explained by an electrical equivalent circuit consisting of constant phase element and resistance. Also, A. Benali et al. [14] have reported the dielectric properties of $La_{0.8}Ca_{0.2}FeO_3$. They have found that the dielectric relaxation had a thermally activated process with activation energy of 0.236 eV and the non-overlapping small polaron tunneling (NSPT) model was the suitable model to explain the electrical conduction

mechanism. S. Acharya et al. [15] have shown that in $La_{0.5}Al_{0.5}FeO_3$, the variation of dielectric constant with temperature indicates the presence of Maxwell–Wigner type polarization.

In this paper, we propose to study the annealing temperature effect on the structural, morphological and dielectric properties of $La_{0.75}Ba_{0.25}FeO_3$ compound synthesized by sol-gel method.

II. Experimental:

The $\mathbf{La_{0.75}Ba_{0.25}FeO_3}$ powder was synthesized by the sol-gel method, using the citric acid route [16, 17]. Stoichiometric amounts of lanthanum nitrate ($La(NO_3)_3.6H_2O$), barium nitrate ($Ba(NO_3)_2$) and ferric nitrate ($Fe(NO_3)_3.9H_2O$) were firstly dissolved in distilled water to obtain an aqueous solution. Then, citric acid (the molar ratio of the acid to the metallic cations ($(La^{3+} + Ba^{2+} + Fe^{3+})$ was 2 : 1))) was incorporated and dissolved under magnetic stirring for 1 h, at room temperature. Afterward, ethylene glycol ($C_2H_2O_2$) was added to the mixture in a molar ratio citric acid: ethylene glycol of 4:10. Details of the preparation have been described elsewhere [18]. The powders obtained are pressed into pellets of 8 mm and sintered at 800 °C then at 900 °C for 24 hours. In order to study the effect of the annealing temperature on the structural, morphologic and dielectric properties, these same pellets (after an annealing at 900 °C (**LBFO900**)) are annealed at lower temperature of 1100 °C (**LBFO1100**) for 24 hours.

The samples structure was characterized by X-ray powder diffraction (XRD) measurements using X'Pert PRO MPD Diffractometer with copper anticathode (λ =1. 5405 Å) with double Cu Kα radiation in a wide range of Bragg angles ($15° \leq 2\theta \leq 80°$) for phase purity and lattice parameter determinations . The structure refinement was carried out by the Rietveld analysis of the powder XRD data with the FULLPROF software. The microstructure was observed using a VEGA3 TESCAN scanning electron microscope (SEM). Before observation all samples were sputtered with carbon to improve conductivity. For dielectric measurements the

samples were placed between two parallel plate electrodes. The impedance spectroscopy measurements were carried out over a frequency range from 100 Hz to 1 MHz at various temperatures (in the range from 150 K to 350 K), using an Agilent 4294 A Precision impedance analyzer, measuring in the Cp–Rp configuration.

III. Results and discussion:

III.1 Structural and morphology properties:

The X-ray diffraction (XRD) pattern of LBFO900 and LBFO1100 measured at room temperature are shown in **Fig.1 (a)** and **(b)**. The Rietveld refinements of the XRD data, with the Fullprof software, shows that both samples crystallized in the orthorhombic structure with the Pnma space group. The results of refinement are summarized in **Table I**, and they are in good agreement with literature **[19]**.

Average crystallite size for the both samples was determined from full width at half maximum (FWMH) of more intense XRD peaks using Scherer's formula **[20]**:

$$D_{SC} = \frac{k \times \lambda}{\beta \times \cos(\theta)} \quad \textbf{(Eq. 1)}$$

In this equation, k represents the shape factor, λ is the wavelength of X-rays used, β is full width at half maximum and θ is the diffraction angle for the most intense peak. The obtained values of crystallite (D_{SC}) size are 24 and 41 nm for LBFO900 and LBFO1100, respectively, i.e., increasing with the rise of the annealing temperature.

Fig.2(a) and **(c)** show the scanning electron microscopy (SEM) images of the LBFO900 and LBFO1100 samples, respectively. As it can be seen, all particles have almost spherical shapes. The powder annealed at 900 °C is characterized by a relatively narrow particles size distribution with mean diameter about 60 nm (**Fig.2 (b)**). For the powder sintered at 1100 °C, the particle size distribution becomes broader and the mean particle size increases to 250 nm (**Fig.2 (d)**) **[14]**. It is noteworthy that the average particle size, generally known as grain size,

was greater than the average crystallite size obtained by XRD (**Table I**) as expected indicating crystallite aggregation thermal activated.

III.2. Impedance spectrum analysis:

The impedance spectroscopy is an important method to study the electrical properties of ferrites as the impedance of grains can be separated from the other impedance sources, such as impedance of electrodes and grain boundaries **[21]**. Complex impedance spectroscopy of a material can be described by the following equation:

$$Z^* = Z' - jZ'' \quad \text{(Eq. 2)}$$

Where Z' and Z'' are ascribed to real and imaginary parts of impedance. **Fig. 3 (a)** and **(b)** displays the variation of the real part of impedance with the frequency of the LBFO900 and LBFO1100, respectively. For both samples, It is clear from these curves that the values of Z' are higher at low frequency region. Then, this values decreases gradually with increasing frequency which allowsan increase in conductivity. This behavior is mainly due to the increase of the charges carriers mobility and a decrease of the density of trapped charges **[22]**. However, at higher frequencies, the impedance (Z') curves of our samples are merged indicating a possible release of a space charge as a result of the lowering of the barrier properties of the materials at higher temperatures and can be interpreted by the presence of space charge polarization **[23]**. It is clearly seen that all values of the real part of impedance decreases with increasing the heat treatment of the sample from 900 °C to 1100 °C.

The variation of the imaginary part of impedance with frequency at different temperatures has been studied and the results are shown in **Fig.4 (a)** and **(b)** for LBFO900 and LBFO1100. For both treatments, the spectra of Z'' are characterized by the appearance of the peaks Z''_{max}, which indicates the presence of relaxation phenomenon in our materials **[24]**. The values of the Z''_{max} shift to higher frequencies with increasing temperatures, that are provided by the

increase of the relaxation time and this shows that the resistance of the bulk material is decreasing [23]. A significant broadening of the peaks with increasing in temperature suggests the existence of a temperature-dependent relaxation phenomenon. Further, the magnitude of Z'' decreases gradually when the temperature increases. This may be due to an accumulation of space charges in LBFO [25]. In order to explain the effect of the annealing temperature, we show in Fig.5 the normalized spectrum of Z'' (i.e. Z''/Z''_{max}) as a function of frequency at 200, 250, and 350 K of both samples annealed at 900 and 1100 °C. It is clearly seen that the weak shift in frequency after annealing has been observed for several temperatures. The frequency (f_{max}) at which the maximum of Z'' occurs may be expressed by the Arrhenius law:

$$f_{max} = f_0 \exp\left(-\frac{E_a}{k_B T}\right) \quad \text{(Eq. 3)}$$

Where f_0, E_a and k_B are the pre-exponential term, the activation energy and the Boltzmann constant, respectively. The temperature dependence of the relaxation frequency is shown in Fig. 6 and the values of the activation energy were estimated from the slope of the linear fit plot. It can be seen from this figure that the activation energy is E_a=0.289 eV for LBFO900 and E_a=0.278 eV for LBFO1100. Thus, we conclude that the activation energy decreases with increasing of sintering temperature.

Fig.7 (a) and (b) represents the complex impedance plots of Z'' versus Z' (Nyquist plots) of LBFO900 and LBFO1100, respectively. The impedance spectra are characterized by the appearance of semicircular arcs whose radii of curvature decrease with increasing temperature, this behavior indicates a decrease in relaxation time [26]. To analyze these impedance spectra, the data was fitted using Z-view software in which we have used an equivalent circuit, as shown in the inset in Fig. 7. The adequate equivalent circuit is composed by a series array of two circuits, one represents grain boundaries (R_1-CPE circuit) where CPE

is a constant phase element and the other (R_2-C circuit) where C is a capacitor represents grain effects. The CPE impedance (Z_{CPE}) is given by the following relation:

$$Z_{CPE} = \frac{1}{Q(j\omega)^{\alpha}} \quad \textbf{(Eq. 4)}$$

Where Q is a proportional factor, ω is the angular frequency, and α is the parameter which estimates the deviation from the ideal capacitive behavior, α is zero for the pure resistive behavior and is the unit for the capacitive. The real Z' and imaginary Z'' parts of the total impedance of the equivalent circuit can be expressed by the following relationships:

$$Z^{*} = Z' - jZ'' = \frac{1}{R_{gb}^{-1} + Q(j\omega)^{\alpha}} + \frac{1}{R_{gb}^{-1} + j\omega C} \quad \textbf{(Eq. 5)}$$

Where:

$$Z' = \frac{R_{gb}\left(1 + R_{gb}Q\omega^{\alpha}\cos\left(\frac{\alpha\pi}{2}\right)\right)}{\left(1 + R_{gb}Q\omega^{\alpha}\cos\left(\frac{\alpha\pi}{2}\right)\right)^{2} + \left(R_{gb}Q\omega^{\alpha}\sin\left(\frac{\alpha\pi}{2}\right)\right)^{2}} + \frac{R_{gb}}{1 + (\omega R_{gb}C)^{2}} \quad \textbf{(Eq. 6)}$$

$$Z'' = \frac{R_{gb}^{2}Q\omega^{\alpha}\sin\left(\frac{\alpha\pi}{2}\right)}{\left(1 + R_{gb}Q\omega^{\alpha}\cos\left(\frac{\alpha\pi}{2}\right)\right)^{2} + \left(R_{gb}Q\omega^{\alpha}\sin\left(\frac{\alpha\pi}{2}\right)\right)^{2}} + \frac{\omega R_{gb}^{2}C}{1 + (\omega R_{gb}C)^{2}} \quad \textbf{(Eq. 7)}$$

The parameters R_g, R_{gb}, C, Q (CPE) and α, are obtained from the fit of experimental data and then are summarized in **Table II** for both samples LBFO900 and LBFO1100. It was found that the resistance values of both grain and grain boundary decreases with increasing temperature, which can be explained by an increase of the mobility of charges carriers that adds to the conduction process **[27]**. This indicates that our samples have a semiconductor behavior. We noted, here, that the grain boundary resistances (R_{gb}) values are larger than the grain ones (R_g). This is assigned to the fact that the atomic arrangement near the grain boundary region is disordered, resulting in a serious increase in electron scattering. On the

other hand, we have found that the increase in annealing temperature from 900 °C to 1100 °C is accompanied by decreases in grain and grain boundary resistances and an increase in CPE. The representation of the logarithmic variation of two resistances (R_{gb}) and (R_g), in **Fig.8(a)** and **(b)** for both samples LBFO900 and LBFO1100, as a function of $10^3/T$ leads to two straight lines, which means that R_{gb} and R_g follow the Arrhenius law:

$$R_{gb,g} = R_0 \exp\left(\frac{E_a}{k_B T}\right) \quad \textbf{(Eq. 8)}$$

Where R_0 represents the pre-exponential constant or characteristic resistance, k_B is the Boltzmann constant, and E_a is the activation energy. When the annealing temperature increases from 900 °C to 1100 °C, it is found that E_a decreases slightly and the activation energy for grain boundary resistance (0.273 eV) was found to be larger than the grain resistance (0.249 eV).

III.3. Dielectric Modulus Analysis:

Complex modulus spectrum could distinguish against the grain, grain boundary and interface or electrode contributions and indicates the electrical phenomenon occurring in the dielectric spectrum. The variation of the real M' (bottom panel) and imaginary M'' (top panel) parts of the complex electrical modulus as a function of the frequency over the temperature range of 150 to 350 K are given in **Fig.9 (a)** and **(b)** for both samples LBFO900 and LBFO1100, respectively.

It is clearly observed in **Fig. 9(a)** that real modulus M' shows dispersion as the frequency is increased and then shows a plateau at higher frequencies. The small value of M' in the low frequency region facilitates the migration of ion conduction. It is also observed in **Fig. 9(a)** that the imaginary modulus M'' exhibits a single relaxation peak. This relaxation peak tends to move to higher frequencies with increasing temperature in the dispersion region of M'. The frequency region below the peak maximum is where the charge carriers are mobile over long

distances. At frequencies above the peak maxima is where the carriers are spatially confined to their potential wells, being mobile on short distance [28]. As the temperature is increased, the movement of the charge carriers becomes faster and consequently they possess decreased relaxation time and hence shift of the peak value towards higher frequencies observed. Thus, it can be concluded that the relaxation process is thermally activated [29].

When the increasing of the annealing temperature from 900 °C to 1100 °C, two peaks are observed in **Fig. 9(b),** at low temperature, indicating the presence of two relaxation processes in LBFO1100. At low frequency, the peak corresponds to the relaxation of the grain boundary and at high frequency; it corresponds to the grain [30]. Then, the two peaks of M'' shift to the higher frequency with increasing the temperature.

To more understand the effect of annealing temperature on the electrical properties of both samples LBFO900 and LBFO1100, we report in **Fig. 10 (a)** and **(b)** the complex plane plot M'' versus M' (Argand's plot) at selected temperature (200 K and 250 K), we observe that the modulus plane shows a single relaxation peak for LBFO900. When the annealing temperature increase to 1100 °C, it is noteworthy an appearance of two relaxations, for LBFO1100, clearly separated from each other: one corresponds to grain boundary and the other to grain effects.

III.4. AC Electrical conductivity analysis:

Electrical conduction in dielectrics is due to the ordered motion of loosely bound charge particles due to the influence of an electric field. Hence, the study of electrical conductivity with frequency and temperature is very important to visualize the effect of these defects on conduction process. The frequency response of ac conductivity at several temperatures for both samples LBFO900 and LBFO1100 are shown in **Fig.11 (a)** and **(b)**, respectively. When the annealing temperature increases, we can see an increase in conductivity as a function of temperature and frequency. From the **Fig.11,** for the both samples, one can also observe that the spectra of the electrical conductivity can be divided into two parts; an independent part of

the frequency (at low frequencies), considered as the dc conductivity, and a highly dispersive part considered as an ac conductivity [31, 32]. The relation between σ_{dc} and σ_{ac} can be expressed as a function of the Jonscher law [33]:

$$\sigma_{ac} = \sigma_{dc} + A\omega^{S} \quad \text{(Eq. 9)}$$

Where, σ_{ac} is the alternative current conductivity, σ_{dc} is the direct current conductivity of the sample and ω is the angular frequency of measurement. The exponent **"S"** represents the degree of interaction between mobile ions with the lattices around them and A is a constant which determines the strength of polarizability. The σ_{dc} at different temperatures can be obtained according to a nonlinear fitting based on **Eq (9)** and the adjusted results of the electrical conductivity are summarized in **Table III**. According to Funke [34], the value of S could have a physical significance; if S<1, the load carriers adopt a translational movement with a sudden jump, and when S> 1 means a localized jump of the species (small jump without leaving the neighborhood). To determine the conduction mechanism of the ac conductivity for both samples LBFO900 and LBFO1100, the variation of the **"S"** exponent as a function of the temperature is shown in **Fig.12**. We found that the S parameter is strongly depending on temperature for both samples.

By correlating the conduction mechanism of Ac conductivity with the **S (T)** behavior one can suggest the appropriate model for the predominant conduction mechanism of the Ac conductivity [35].

In the literature, different models have been considered based on two distinct processes, namely, classical hopping over a barrier and quantum-mechanical tunneling, or some variant or combination of the two, and it has been differently assumed that electrons (or polarons) or atoms are the carriers responsible [36].

These different models are:

- The **Q**uantum **M**echanical **T**unneling (QMT) model, the exponent "S" is virtually equal to 0.8 and independent of temperature or increases slightly with temperature [37, 38].
- The **C**orrelated **B**arrier **H**opping (CBH) model, the exponent "S" decreases with the increase in temperature [39].
- The **O**verlapping **L**arge-**P**olaron **T**unneling (OLPT) model, the exponent "S" depends on both temperature and frequency and drops with increasing temperature to a minimum value and then rises when the temperature increases [40].
- The **N**on-overlapping **S**mall **P**olaron **T**unneling (NSPT) model, the exponent "S" is temperature dependent. It increases with the increase in temperature [37].

So, the results of the "S" parameter suggest that the OLPT and NSPT models are the most suitable models to characterize the electrical conduction mechanism in the LBFO900 and the LBFO1100 oxides compounds, respectively. We can conclude that the heat preparation temperature of the LBFO sample influence largely on the conduction mechanism.

To study the conductivity mechanism at low frequencies we plot in **Fig.13** Ln (σ_{dc}T) vs 10^3/T for both samples LBFO900 and LBFO1100. The plots were well fitted by the Mott and David law which describe small polaron hopping [41]:

$$\sigma_{dc} = \sigma_0 \exp\left(-\frac{E_a}{k_B T}\right) \quad \textbf{(Eq. 10)}$$

Where σ_0 is a pre-exponential factor and E_a is the activation energy. The linear behavior of Ln (σ_{dc}T) *vs* 10^3/T suggests that conducting processes is thermally activated [42]. The E_a estimated from the slope of the linear fit plots have almost the same values 0.289 eV and 0.285 eV for LBFO900 and LBFO1100, respectively.

We examined the grain and grain boundary conductivity for both samples LBFO900 and LBFO1100, using the following equations [23]:

$$\sigma_g = \frac{e}{S_f \times R_g} \quad \textbf{(Eq. 11)}$$

$$\sigma_{gb} = \frac{e}{S_f \times R_{gb}} \textbf{(Eq. 12)}$$

Where, *e* is the thickness of pellet, S_f is its area, R_g is the grain resistance and R_{gb} is the grain boundary resistance of the samples, calculated in the above section. The conductivity values for the grain and the grain boundary for the two compounds are summarized in the **Table IV**. It's noteworthy that the σ_g and σ_{gb} conductivity increases with rise in temperature for both samples. Furthermore, we notice that the grain conductivity values are larger than that of the grain boundary, indicating that the conductivity of the material is ensured by the grains more than grain boundaries. For LBFO1100, the values of grain boundary and grain conductivity are greater than those for LBFO900.

Finally, in this work, we have shown that the annealing temperature greatly affects the electrical properties of the $La_{0.75}Ba_{0.25}FeO_3$ compound. Indeed the compound annealed at 1100°C is more conductive than that annealed at 900°C and that these two samples have different conduction mechanisms. This could be explained by the increase of the grain size with the annealing temperature which favors the conduction both within the grain and through the grain boundaries.

IV. Conclusion:

The annealing temperature effect from 900 to 1100 °C on morphology and dielectric properties of $La_{0.75}Ba_{0.25}FeO_3$ prepared by sol-gel has been investigated. SEM images have been shown that the mean grain size increases from 60 to 250 nm with increasing of annealing temperature from 900 to 1100 °C. Then, electric modulus results have been shown two relaxations attribute to grain boundary and gain contributions at low and high frequency,

respectively, at high annealing temperature. The two relaxations shift to higher frequencies when the temperature increases from 150 to 350 K. The ac conductivity analysis shows that the annealing temperature affect the conduction mechanism model; the suitable model for the LBFO900 sample is the OLPT model while it's the NSPT model for the LBFO1100 sample.

References:

[1] K. Huang, H.Y. Lee, J.B. Goodenough, J. Electrochem. Soc. **145** (1999) 3220.

[2] M.H. Hung, M.V.M. Rao, D.S. Tsai, Mater. Chem. Phys. **101** (2007) 297.

[3] A. Delmastro, D. Mazza, S. Ronchetti, M. Vallino, R. Spinicci, P. Brovetto, M. Salis, Mater. Sci. Eng. B **79** (2001) 140.

[4] N.N. Toan, S. Saukko, V. Lantto, Physica B **327** (2003) 279.

[5] V. Lantto, S. Saukko, N.N. Toan, L.F. Reyes, C.G. Granqvist, J. Electroceram. **13** (2004) 721.

[6] D. Wang, M. Gong, J. Appl. Phys. **109** (2011) 114304.

[7] S. Phokha, S. Pinitsoontorn, S. Rijirawat, S. Maensiri, J. Nanosci. Nanotechnol. **15** (2015) 9171.

[8] V.V. Kharton, A.P. Viskup, E.N. Naumovich, V.N. Tikhonovich, Mater. Res. Bull. **34** (1999) 1311.

[9] J. E. ten Elshof, M. H. R. Lankhorst, H. J. M. Bouwmeester, J. Electrochem. Soc. **144** (1997) 1060.

[10] M.A. Ahmed, A.A. Azab, E.H. El-Khawas, J. Mater. Sci. Mater. Electron. **26** (2015) 8765.

[11] M. W. Khan, S. Husain, M. A. M. Khan, M. Gupta, R. Kumar, J. P. Srivastava, Philos. Mag. **90** (2010) 3069.

[12] C. Chen, K.B. Xu, Y.M. Cui, C.C. Wang, Mater. Lett. **89** (2012) 153.

[13] S. Chanda, S. Saha, A. Dutta, B. Irfan, R. Chatterjee, T.P. Sinha. J. Alloys Compd. **649** (2015) 1260.

[14] A. Benali, A. Souissi, M. Bejar, E. Dhahri, M.F.P. Graça¸ M.A. Valente, Chem. Phys. Lett. **637** (2015) 7.

[15] S. Acharya, P.K. Chakrabarti, Solid State Commun. **150** (2010) 1234.

[16] M.P.F. Graça, P.R. Prezas, M.M. Costa, M.A. Valente, J. Sol-Gel Sci. Technol. **64** (2012) 78.

[17] A. Benali, M. Bejar, E. Dhahri, M. Sajieddine, M.P.F. Graça, M.A. Valente, Mater. Chem. Phys. **149-150** (2015) 467.

[18] A. Benali, S. Azizi, M. Bejar, E. Dhahri, M.F.P. Graça, Ceram. Int. **40** (2014)14367.

[19] L. Sun, H. Qin, K. Wang, M. Zhao, J. Hu, Mater. Chem. Phys. **125** (2011) 305.

[20] F. Elleuch, M. Triki, M. Bekri, E.Dhahri, E.K. Hlil, J. Alloys Compd. **620** (2015) 249.

[21] K.M. Batoo, Physica B **406** (2011) 382.

[22] E. Barsoukov, J.R. Macdonald, Impedance Spectroscopy Theory, Experiment, and Applications, 2nd ed., John Wiley and Sons, New York (2005).

[23] A. Benali, M. Bejar, E. Dhahri, M.F.P. Graça, L.C. Costa. J. Alloys Compd. **653** (2015) 506.

[24] S. Hcini, A. Selmi, H. Rahmouni, A. Omri, M.L. Bouazizi, Ceram. Int. **43** (2017) 2529.

[25] A.R. James, K. Srinivas, Mater. Res. Bull. **34** (1999) 1301.

[26] C.Y. Tsay, Y.H. Lin, Y.M. Wang, H.Y. Chang, C.M. Lei, S.U. Jen, AIP Adv. **6** (2016) 055909.

[27] H. Trabelsi, M. Bejar, E. Dhahri, M. Sajieddine, K. Khirouni, P.R. Prezas, B.M.G. Melo, M.A. Valente, M.P.F. Garça. J. Alloys Compd. **723** (2017) 894.

[28] K. Holderna-Natkaniec, M.O.M. Sghaier, P. Ławniczakc, M. Zdanowska-Fraczek, A. Wozniak-Braszak, S. Chaabouni, Polyhedron **85** (2015) 131.

[29] J.S .Kim, J. Phys. Soc. Jpn. **70** (2001) 3129.

[30] C. Ben Mohamed, K. Karoui, S. Saidi, K. Guidara, A. Ben Rhaiem, Physica B **451** (2014) 87.

[31] N. Chihaoui, M. Bejar, E. Dhahri, M.A. Valente, L.C. Costa, M.P.F. Graça, International Journal of Materials Engineering and Technology **13** (2015) 129.

[32] A.R. James, C. Prakash, G. Prasad, J. Phys. D: App. Phys. **39** (2006) 1635.

[33] A.K. Jonscher, Universal Relaxation Law, Chelsea Dielectric Press, London (1996).

[34] K. Funke, Prog. Solid State Chem. **22** (1993) 111.

[35] S. R. Elliot, Adv. Phys. **36** (1987) 135.

[36] M. Ben Bechir, K. Karoui, M. Tabellout, K. Guidara, A. Ben Rhaiem, J. Alloys Compd. **588** (2014) 551.

[37] A. Ghosh, Phys. Rev. B **41** (1990) 1479.

[38] M. Pollak, Philos. Mag. **23** (1971) 519.

[39] S. Mollah, K. K. Som, K. Bose, B. K. Chaudhuri, J. Appl. Phys. **74** (1993) 931.

[40] M. Megdiche, C. Perrin–pellegrino, M. Gargouri, J. Alloys Compd. **584** (2014) 209.

[41] D.K. Mahato, T.P. Sinha, J. Alloys Compd. **634** (2015) 246.

[42] A. Omri, M. Bejar, E. Dhahri, M. Es-Souni, M.A. Valente, M.P.F. Graça, L.C. Costa. J. Alloys Compd. **536** (2012) 173.

Figures captions:

Figure 1: Rietveld refinement plot for LBFO900 (a) and LBFO1100 (b) samples.

Figure 2: SEM micrographs ((a) and (c)) and corresponding histogram plot ((b) and (d)) for particle size distributions of the LBFO900 and LBFO1100 samples.

Figure 3: Variation of real ($Z^{'}$) part of the impedance as a function of the frequency at various temperatures of the LBFO900 (a) and LBFO1100 (b) samples.

Figure 4: Variation of real ($Z^{''}$) part of the impedance as a function of the frequency at various temperatures of the LBFO900 (a) and LBFO1100 (b) samples.

Figure 5: Frequency dependence of normalized peak $Z^{''}/Z_{max}^{''}$ at different temperatures of the LBFO900 and LBFO1100 samples.

Figure 6: The Arrhenius plots shows depedence f_{max} versus 10^3/T for LBFO900 and LBFO1100 samples.

Figure 7: Nyquist plot at various temperatures and equivalent circuit (fitting data) of the LBFO900 (a) and LBFO1100 (b) samples.

Figure 8: The Arrhenius plots shows depedence resistances grain (R_g) and grain boundary (R_{gb}) versus 1/T of the LBFO900 (a) and LBFO1100 (b) samples.

Figure 9: Variation of the real $M^{'}$ (bottom panel) and imaginary $M^{''}$ (top panel) parts of the electrical modulus as a function of the frequency at various temperatures of the LBFO900 (a) and LBFO1100 (b) samples.

Figure 10: Argand plot for electric modulus ($M^{''}$ vs $M^{'}$) at 200 K and 250 K of the LBFO900 (a) and LBFO1100 (b) samples.

Figure 11: Variation of the ac conductivity as a function of the frequency at various temperatures of the LBFO900 (a) and LBFO1100 (b) samples.

Figure 12: Temperature variation of fitted power exponent S parameter using Jonscher law for LBFO900 and LBFO1100 samples.

Figure 13: Variation of the $Ln(\sigma_{dc}T)$ as a function $10^3/T$for LBFO900 and LBFO1100 samples.

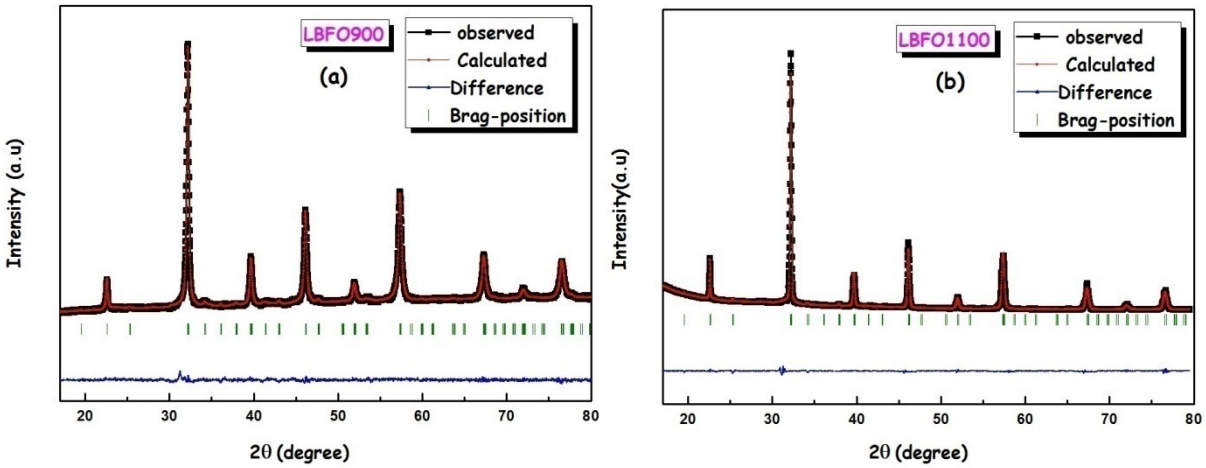
LBFO900
(a)
observed
Calculated
Difference
Brag-position
Intensity (a.u)
2θ (degree)
LBFO1100
(b)
observed
Calculated
Difference
Brag-position
Intensity(a.u)
2θ (degree)

Fig.1

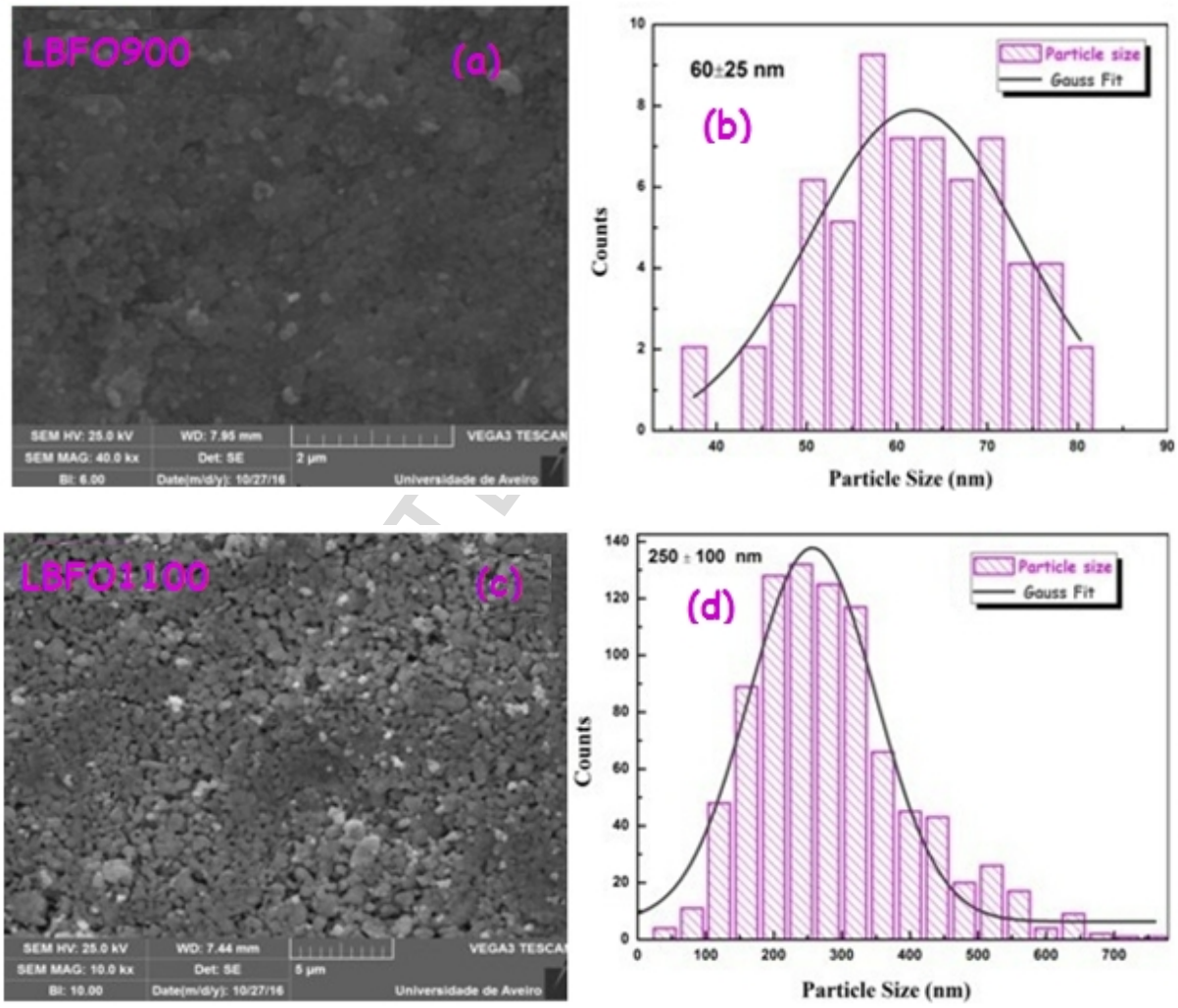
LBFO900
(a)
SEM HV: 25.0 kV
WD: 7.95 mm
VEGA3 TESCAN
SEM MAG: 40.0 kx
Det: SE
2 μm
Bl: 6.00
Date(m/d/y): 10/27/16
Universidade de Aveiro
60±25 nm
(b)
Particle size
Gauss Fit
Counts
Particle Size (nm)
LBFO1100
(c)
SEM HV: 25.0 kV
WD: 7.44 mm
VEGA3 TESCAN
SEM MAG: 10.0 kx
Det: SE
5 μm
Bl: 10.00
Date(m/d/y): 10/27/16
Universidade de Aveiro
250 ± 100 nm
(d)
Particle size
Gauss Fit
Counts
Particle Size (nm)

Fig.2

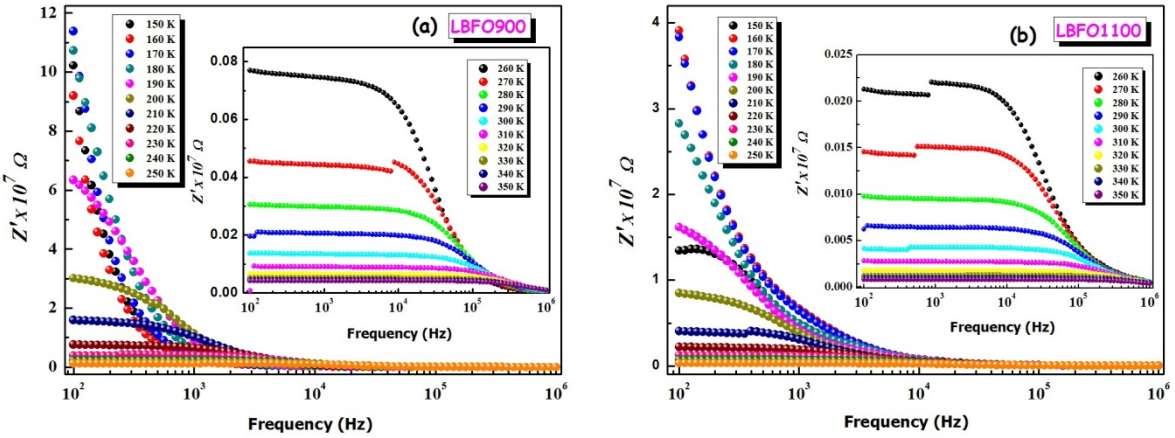

Fig.3

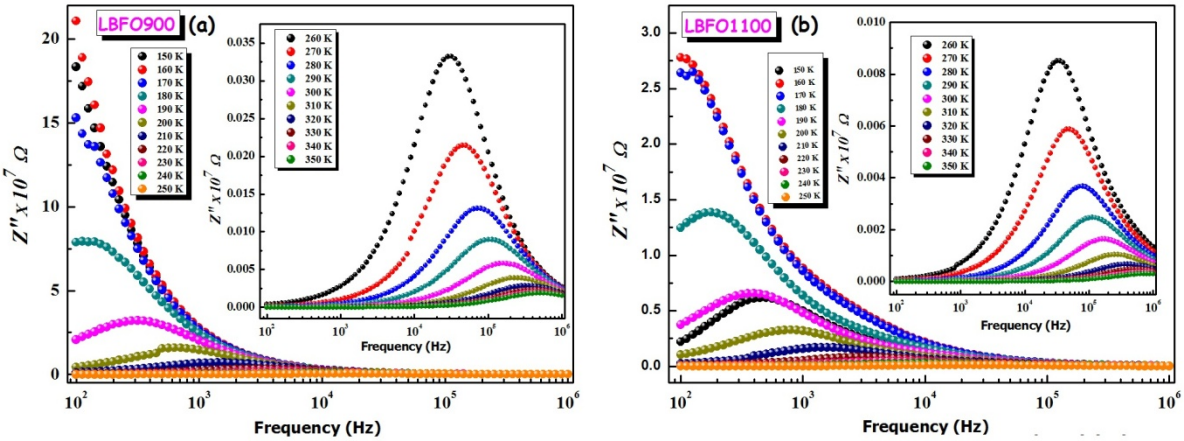

Fig.4

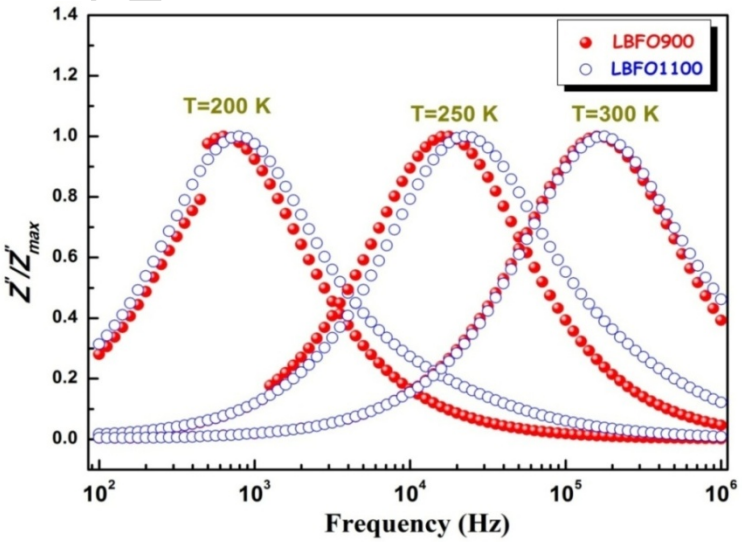

Fig.5

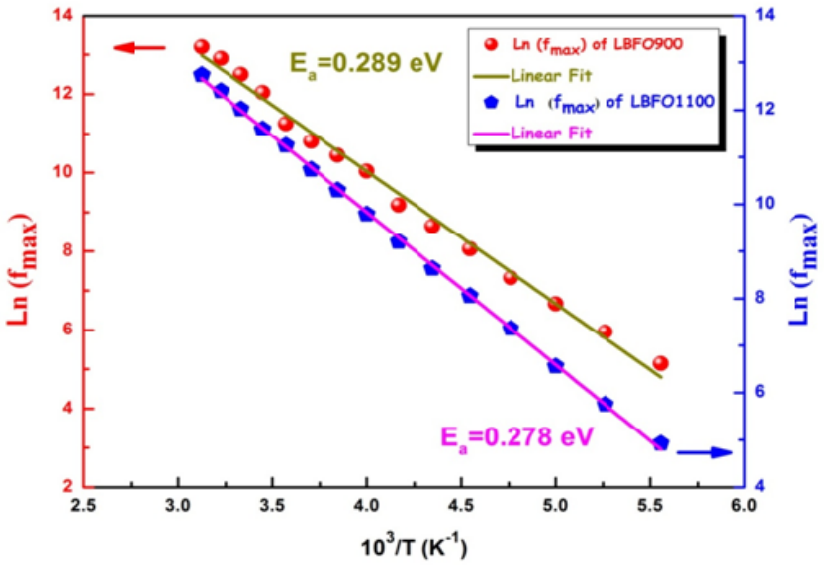

Fig.6

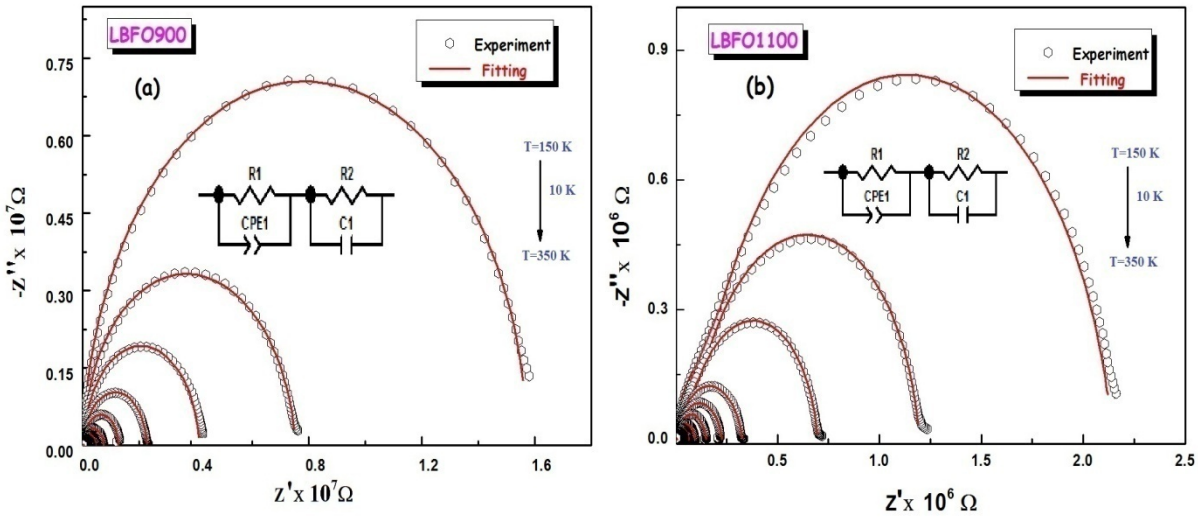

Fig.7

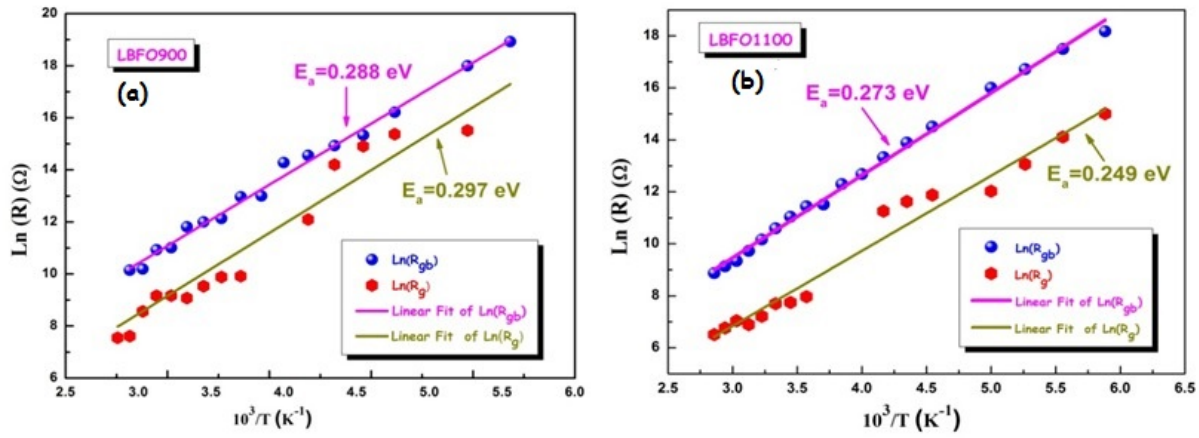

Fig.8

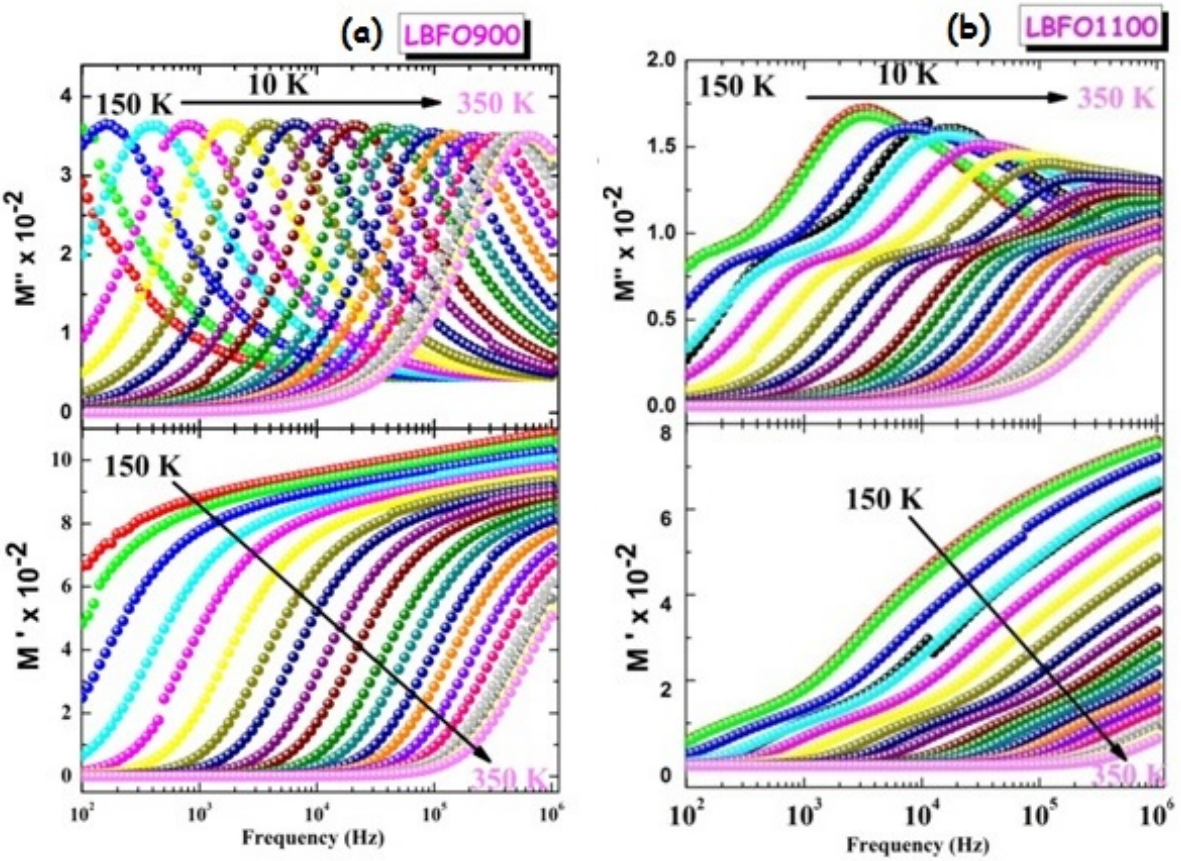
(a)
LBFO900
150 K
10 K
350 K
M" x 10-2
M ' x 10-2
150 K
350 K
Frequency (Hz)
(b)
LBFO1100
150 K
10 K
350 K
M" x 10-2
M ' x 10-2
150 K
Frequency (Hz)

Fig.9

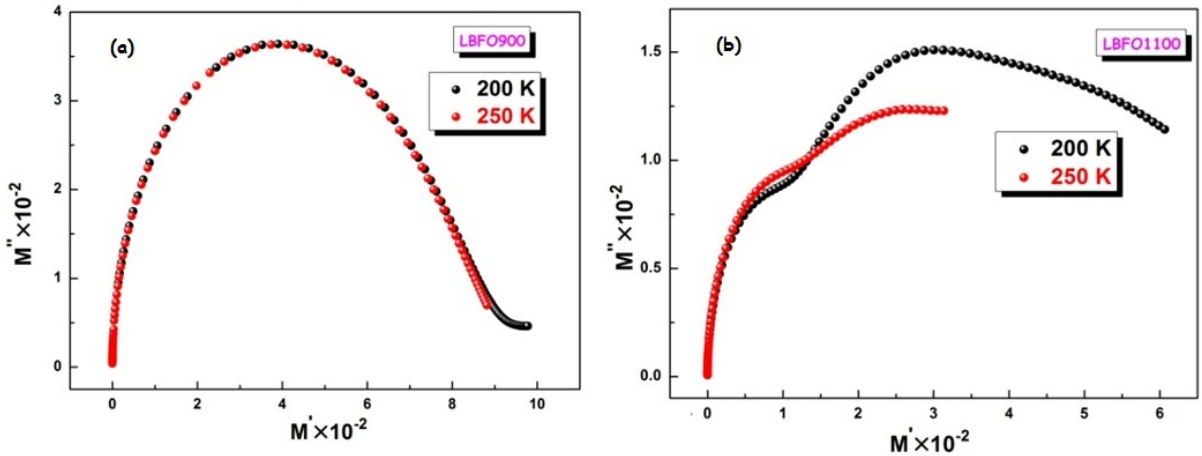
(a)
LBFO900
200 K
250 K
M"×10-2
M'×10-2
(b)
LBFO1100
200 K
250 K
M"×10-2
M'×10-2

Fig.10

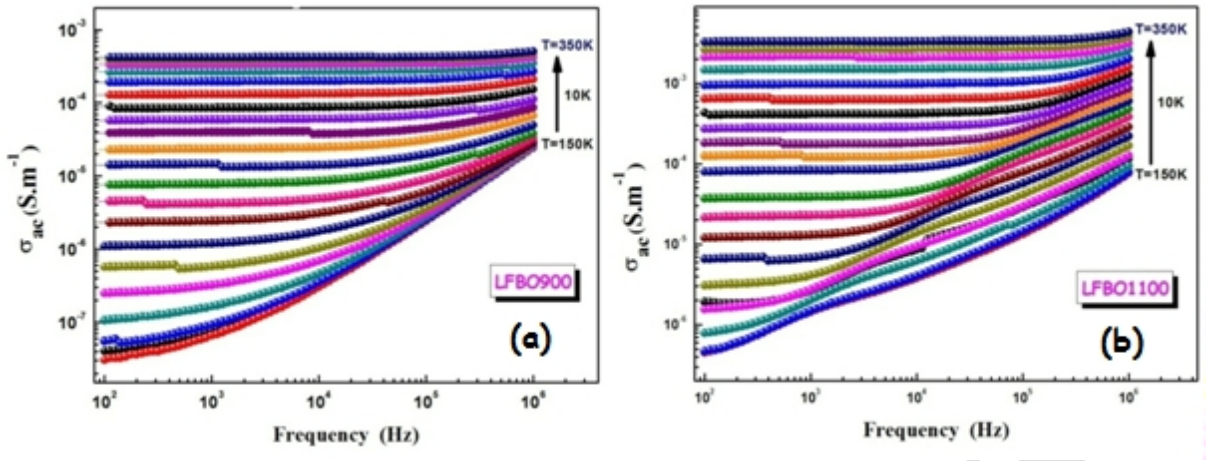

Fig.11

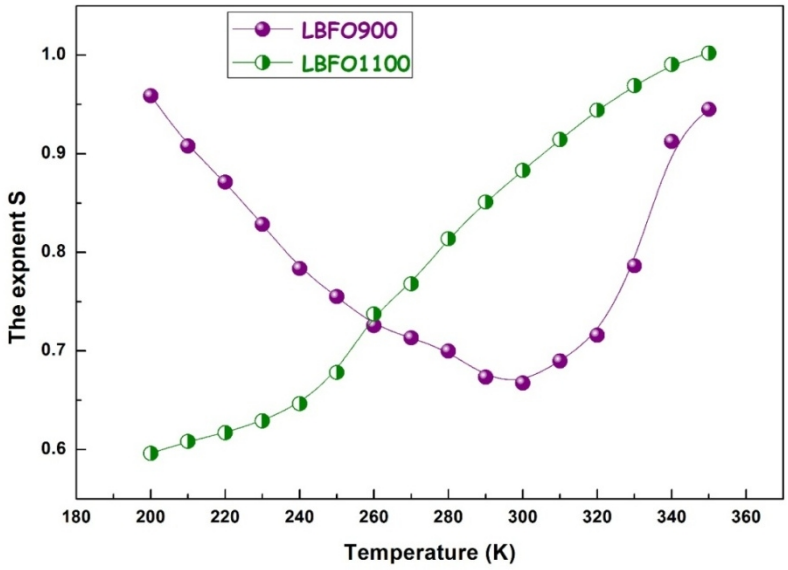

Fig.12

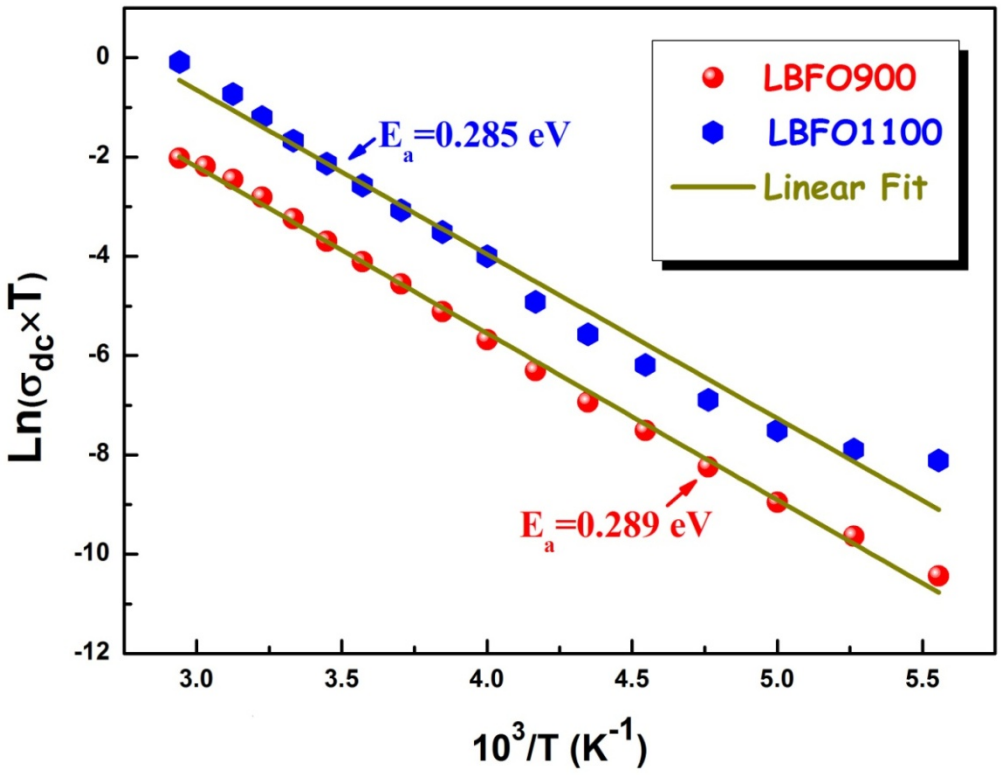

Fig.13

Highlights:

- The $La_{0.75}Ba_{0.25}FeO_3$ compound was synthesized using the sol-gel method.
- The annealing temperature effect from 900 to 1100 °C on morphology and dielectric properties of $La_{0.75}Ba_{0.25}FeO_3$ has been investigated.
- The conductivity has been investigated by the Jonscher universal power law.

List of tables:

Table I

		LBFO900	LBFO1100
Space group		Pnma	Pnma
Lattice parameters (Å)	a	5.559	5.553
	b	7.867	7.865
	c	5.568	5.561
Cell Volume ($Å^3$)		243.503	242.783
Crystallite size (nm)		24	41
Grain size (nm)		60 ± 25	250 ± 100

Table II

T(K)	R_{gb} (MΩ)		CPE (pF)		alpha		R_g (MΩ)		C (pF)	
	900 °C	1100 °C	900 °C	1100 °C	900 °C	1100 °C	900 °C	1100 °C	900 °C	1100 °C
150	688.71	140	8.516	68.77	0.9688	0.899	8.993	4.477	54.38	10.27
160	503.13	82.17	8.127	92.32	0.9664	0 .811	8.426	3.634	61.88	10 .18
170	358	78.68	8.033	130.7	0.9688	0.776	8.145	3.288	76.96	10.1
180	164.91	39.82	9.563	141.1	0.9649	0.782	6.1933	1.349	39	24.6
190	65.67	18.34	11.28	156.5	0.9594	0.779	5.459	0.473	28.38	32.4
200	30.16	8.892	68.62	155.3	0.9053	0.791	28.93	0.166	7.563	35.51
210	14.64	1.933	17.71	72 .32	0.9562	0.833	4.752	0.149	40.15	12 .21
220	10.05	1.864	33.01	87.39	0.9209	0.809	2.985	0.144	17.57	13.65
230	3.038	1.086	17.36	87.32	0.9459	0.908	1.464	0.112	18.47	14.24
240	2.097	0.622	13.73	87.39	0.9531	0.916	0.178	0.077	34.01	15.65
250	1.592	0.323	59.41	160.1	0.915	0.8318	1.099	0.054	8.783	42.5
260	0.441	0.221	61.13	201.2	0.8903	0.838	0.330	0.051	12.1	34.25
270	0.425	0.097	93.89	361.1	0.984	0.879	0.022	0.048	29.42	88.71
280	0.192	0.093	86.64	161.8	0.9876	0.848	0.019	0.0033	41.08	78.34
290	0.166	0.062	24.14	144	0.9236	0.863	0.013	0.001	11.77	21.69
300	0.132	0.039	22.75	99.59	0.9187	0.892	0.009	0.002	41.55	16.5
310	0.063	0.026	61.19	130.9	0.889	0.877	0.0085	0.001	16.57	18.59
320	0.055	0.016	32.63	132.4	0.9114	0.884	0.0081	9.86E-4	40.62	131.8
330	0.026	0.011	83.46	93.8	0.8753	0.912	0.005	0.00114	31.75	32.9
340	0.025	0.009	64.57	108.4	0.8865	0.899	0.002	8.62E-4	18.47	175.1
350	0.013	0.007	38.15	134	0.9141	0.896	0.0018	6.69E-4	21.03	301

Table III

	LBFO900			LBFO1100		
T (K)	σ_{dc} (10^{-5} S.m^{-1})	A (x10^{-12})	S	σ_{dc} (10^{-5} S.m^{-1})	A (x10^{-12})	S
150	0.0085	3.032	1.015	0.170	83.744	0.805
160	0.0066	2.646	1.024	0.135	2.823	0.795
170	0.0091	3.379	1.009	0.130	4.360	0.771
180	0.0161	4.690	0.989	0.166	17.192	0.694
190	0.0340	5.687	0.978	0.196	50.717	0.644
200	0.0642	7.904	0.958	0.275	106.539	0.614
210	0.1248	17.888	0.907	0.484	156.839	0.607
220	0.248	32.185	0.871	0.932	200.454	0.608
230	0.422	116.95	0.828	1.652	252.865	0.611
240	0.761	350.021	0.783	3.044	216.082	0.635
250	1.368	723.281	0.755	7.352	121.997	0.683
260	2.318	481.255	0.725	11.503	51.188	0.748
270	3.889	54.5336	0.713	17.162	20.901	0.814
280	5.851	926.729	0.699	27.314	8.3751	0.882
290	8.512	528.979	0.673	40.886	2.776	0.959
300	13.043	524.129	0.667	62.668	0.469	1.030
310	19.478	2760.61	0.689	97.258	0.388	1.093
320	26.872	1622.8	0.715	150.423	0.244	1.124
330	33.999	9.6994	0.888	162.32	0 .206	1.175
340	38.683	6.52971	1.027	269.218	0.105	1.223
350	42.114	2.13961	1.146	331.679	0.048	1.180

Table IV

	σ_g (10^{-5} S.m^{-1})		σ_{gb}(10^{-5} S.m^{-1})	
T(K)	900 °C	1100 °C	900 °C	1100 °C
150	0.903	1.814	0.011	0.058
160	0.964	1.452	0.0161	0.098
170	0.997	2.471	0.022	0.103
180	1.311	6.022	0.049	0.204
190	1.488	17.177	0.123	0.443
200	1.338	48.699	0.280	0.913
210	1.709	23.113	0.739	2 .459
220	2.721	56.146	1.788	4.066
230	5.549	72.434	2.674	7.502
240	45.646	104.644	3.874	13.147
250	7.393	147.751	5.103	25.203
260	24.576	156.732	18.390	37.102
270	400.838	165.206	18.965	81.350
280	415.813	2822.160	43.800	87.535
290	593.065	3515.794	50.030	130.406
300	933.908	3699.908	60.634	203.705
310	847.236	5987.472	135.056	312.524
320	854.363	8237.023	146.080	486.381
330	1553.537	7152.288	306.026	711.845
340	4022.277	9422.474	320.512	878.283
350	4298.941	12135.922	327.164	1134.776